PHYSICAL REVIEW D VOLUME 45, NUMBER 5 1 MARCH 1992

Topology of three-jet events in $\bar{p}p$ collisions at $\sqrt{s}=1.8$ TeV

F. Abe,[i] D. Amidei,[d] G. Apollinari,[p] M. Atac,[d] P. Auchincloss,[o] A. R. Baden,[f] N. Bacchetta,[k] M. W. Bailey,[n] A. Bamberger,[d] P. de Barbaro,[o] B. A. Barnett,[h] A. Barbaro-Galtieri,[j] V. E. Barnes,[n] T. Baumann,[f] F. Bedeschi,[m] S. Behrends,[b] S. Belforte,[m] G. Bellettini,[m] J. Bellinger,[u] D. Benjamin,[t] J. Bensinger,[b] A. Beretvas,[d] J. P. Berge,[d] S. Bertolucci,[e] S. Bhadra,[g] M. Binkley,[d] R. Blair,[a] C. Blocker,[b] V. Bolognesi,[m] A. W. Booth,[d] C. Boswell,[h] G. Brandenburg,[f] D. Brown,[f] E. Buckley-Geer,[q] H. S. Budd,[o] G. Busetto,[k] A. Byon-Wagner,[d] K. L. Byrum,[u] C. Campagnari,[c] M. Campbell,[c] A. Caner,[d] R. Carey,[f] W. Carithers,[j] D. Carlsmith,[u] J. T. Carroll,[d] R. Cashmore,[d] A. Castro,[k] F. Cervelli,[m] K. Chadwick,[d] G. Chiarelli,[e] W. Chinowsky,[j] S. Cihangir,[d] A. G. Clark,[d] D. Connor,[l] M. Contreras,[b] J. Cooper,[d] M. Cordelli,[c] D. Crane,[d] M. Curatolo,[c] C. Day,[d] F. DeJongh,[d] S. Dell'Agnello,[m] M. Dell'Orso,[m] L. Demortier,[b] B. Denby,[d] P. F. Derwent,[c] T. Devlin,[q] D. DiBitonto,[r] M. Dickson,[o] R. B. Drucker,[j] K. Einsweiler,[j] J. E. Elias,[d] R. Ely,[j] S. Eno,[c] S. Errede,[g] B. Esposito,[e] B. Flaugher,[d] G. W. Foster,[d] M. Franklin,[f] J. Freeman,[d] H. Frisch,[c] T. Fuess,[d] Y. Fukui,[i] Y. Funayama,[s] A. F. Garfinkel,[n] A. Gauthier,[g] S. Geer,[d] D. W. Gerdes,[c] P. Giannetti,[m] N. Giokaris,[p] P. Giromini,[e] L. Gladney,[l] M. Gold,[j] K. Goulianos,[p] H. Grassmann,[k] C. Grosso-Pilcher,[c] C. Haber,[j] S. R. Hahn,[d] R. Handler,[u] K. Hara,[s] R. M. Harris,[d] J. Hauser,[d] C. Hawk,[q] T. Hessing,[r] R. Hollebeek,[l] P. Hu,[q] B. Hubbard,[j] B. T. Huffman,[n] R. Hughes,[l] P. Hurst,[e] J. Huth,[d] H. Hylen,[d] M. Incagli,[m] T. Ino,[s] H. Iso,[s] H. Jensen,[d] C. P. Jessop,[f] R. P. Johnson,[d] U. Joshi,[d] R. W. Kadel,[j] T. Kamon,[r] S. Kanda,[s] D. A. Kardelis,[g] I. Karliner,[g] E. Kearns,[f] L. Keeble,[r] R. Kephart,[d] P. Kesten,[b] R. M. Keup,[g] H. Keutelian,[d] D. Kim,[d] S. Kim,[s] L. Kirsch,[b] K. Kondo,[s] J. Konigsberg,[f] E. Kovacs,[d] S. E. Kuhlmann,[a] E. Kuns,[q] A. T. Laasanen,[n] J. I. Lamoureux,[u] S. Leone,[m] J. Lewis,[d] W. Li,[a] T. M. Liss,[g] P. Limon,[d] N. Lockyer,[l] C. B. Luchini,[g] P. Lukens,[d] P. Maas,[u] M. Mangano,[m] J. P. Marriner,[d] M. Mariotti,[m] R. Markeloff,[u] L. A. Markosky,[u] R. Mattingly,[b] P. McIntyre,[r] A. Menzione,[m] T. Meyer,[r] S. Mikamo,[i] M. Miller,[c] T. Mimashi,[s] S. Miscetti,[e] M. Mishina,[i] S. Miyashita,[s] Y. Morita,[s] S. Moulding,[b] J. Mueller,[q] A. Mukherjee,[d] L. F. Nakae,[b] I. Nakano,[s] C. Nelson,[d] C. Newman-Holmes,[d] J. S. T. Ng,[f] M. Ninomiya,[s] L. Nodulman,[a] S. Ogawa,[s] R. Paoletti,[m] A. Para,[d] E. Pare,[f] S. Park,[d] J. Patrick,[d] T. J. Phillips,[f] R. Plunkett,[d] L. Pondrom,[u] J. Proudfoot,[a] F. Ptohos,[f] G. Punzi,[m] D. Quarrie,[d] K. Ragan,[l] G. Redlinger,[c] J. Rhoades,[u] M. Roach,[t] F. Rimondi,[d] L. Ristori,[m] T. Rodrigo,[d] T. Rohaly,[l] A. Roodman,[c] W. K. Sakumoto,[o] A. Sansoni,[e] R. D. Sard,[g] A. Savoy-Navarro,[d] V. Scarpine,[g] P. Schlabach,[f] E. E. Schmidt,[d] O. Schneider,[j] M. H. Schub,[n] R. Schwitters,[f] A. Scribano,[m] S. Segler,[d] Y. Seiya,[s] M. Sekiguchi,[s] M. Shapiro,[j] N. M. Shaw,[n] M. Sheaff,[u] M. Shochet,[c] J. Siegrist,[j] P. Sinervo,[l] J. Skarha,[h] K. Sliwa,[t] D. A. Smith,[m] F. D. Snider,[h] L. Song,[l] M. Spahn,[j] P. Sphicas,[d] R. St. Denis,[f] A. Stefanini,[m] G. Sullivan,[c] R. L. Swartz, Jr.,[g] M. Takano,[s] F. Tartarelli,[m] K. Takikawa,[s] S. Tarem,[b] D. Theriot,[d] M. Timko,[r] P. Tipton,[d] S. Tkaczyk,[d] A. Tollestrup,[d] J. Tonnison,[n] W. Trischuk,[f] N. Turini,[m] Y. Tsay,[c] F. Ukegawa,[s] D. Underwood,[a] S. Vejcik III,[h] R. Vidal,[d] R. G. Wagner,[a] R. L. Wagner,[d] N. Wainer,[d] J. Walsh,[l] T. Watts,[q] R. Webb,[r] C. Wendt,[u] H. Wenzel,[m] W. C. Wester III,[j] T. Westhusing,[m] S. N. White,[p] A. B. Wicklund,[a] H. H. Williams,[l] B. L. Winer,[o] J. Wyss,[k] A. Yagil,[d] A. Yamashita,[s] K. Yasuoka,[s] G. P. Yeh,[d] J. Yoh,[d] M. Yokoyama,[s] J. C. Yun,[d] A. Zanetti,[m] F. Zetti,[m] and S. Zucchelli[d]

(CDF Collaboration)

[a]*Argonne National Laboratory, Argonne, Illinois 60439*
[b]*Brandeis University, Waltham, Massachusetts 02254*
[c]*University of Chicago, Chicago, Illinois 60637*
[d]*Fermi National Accelerator Laboratory, Batavia, Illinois 60510*
[e]*Laboratori Nazionali di Frascati, Istituto Nazionale di Fisica Nucleare, Frascati, Italy*
[f]*Harvard University, Cambridge, Massachusetts 02138*
[g]*University of Illinois, Urbana, Illinois 61801*
[h]*The Johns Hopkins University, Baltimore, Maryland 21218*
[i]*National Laboratory for High Energy Physics (KEK), Japan*
[j]*Lawrence Berkeley Laboratory, Berkeley, California 94720*
[k]*Universita di Padova, Istituto Nazionale di Fisica Nucleare, Sezione di Padova, I-35131 Padova, Italy*
[l]*University of Pennsylvania, Philadelphia, Pennsylvania 19104*
[m]*Istituto Nazionale di Fisica Nucleare, University and Scuola Normale Superiore of Pisa, I-56100 Pisa, Italy*
[n]*Purdue University, West Lafayette, Indiana 47907*
[o]*University of Rochester, Rochester, New York 14627*
[p]*Rockefeller University, New York, New York 10021*

[q]Rutgers University, Piscataway, New Jersey 08854
[r]Texas A&M University, College Station, Texas 77843
[s]University of Tsukuba, Tsukuba, Ibaraki 305, Japan
[t]Tufts University, Medford, Massachusetts 02155
[u]University of Wisconsin, Madison, Wisconsin 53706
(Received 3 September 1991)

The production and event topology of three-jet events produced in $p\bar{p}$ collisions at $\sqrt{s}=1.8$ TeV have been studied with the Collider Detector at Fermilab at the Tevatron Collider. The distributions of the three-jet angular variables (ψ^* and $\cos\theta^*$) and of the variables describing the energy sharing between jets (x_3 and x_4) are found to agree well with tree-level QCD calculations. These distributions are predicted to have different shapes for different initial-state subprocesses (quark-antiquark, quark-gluon, and gluon-gluon). The data are consistent with the small expected contribution from quark-antiquark initial states, in agreement with theoretical expectations.

PACS number(s): 13.87.$-$a, 12.38.Qk, 13.85.Hd

I. INTRODUCTION

Jet production is the dominant process in high-transverse-energy hadron-hadron collisions. This process is well described by perturbative QCD in terms of a pointlike scattering cross section convoluted with a pair of parton distribution functions that express the momentum distribution of partons within the proton. The hard-scattering cross section itself can be written as an expansion in the strong coupling constant $\alpha_s(Q^2)$. The leading term in this expansion corresponds to the emission of two partons. The next term includes diagrams where an additional parton is observed in the final state due to gluon radiation (e.g., $gg \rightarrow ggg$). Such diagrams, examples of which are seen in Fig. 1, diverge when any of the three partons become soft or when two of the partons become collinear. Tree-level expressions can be used and compared directly to experiment for configurations where partons or jets are required to be energetic and well separated. These requirements avoid regions where singularities dominate the cross sections.

Nevertheless, artifacts of the singularities in the theory can be found in the behavior of the three-jet differential cross section. The existence of a t-channel pole in the parton scattering amplitude causes a peaking in the c.m. system (c.m.s.) distribution of the leading jet with respect to the beam axis, $\cos\theta^*$. Singularities for configurations where two outgoing partons are collinear result in an increased probability of unequal energy sharing between jets. Divergences resulting from an outgoing parton which is collinear with the beam direction cause structure in the angle between the plane containing the three-jet momenta and the plane containing the beam line and the leading jet, ψ^* (Fig. 2). The dimensionless variables x_3 and x_4 describing the fraction of energy carried by the leading two jets in a three-jet event are also examined, and compared to both phase-space models and models where the subprocesses are separated into different components. Because of the differences in the spins and couplings of quarks to gluons and gluons to gluons, the QCD predictions for these distributions can differ depending on whether one selects subprocesses initiated by gg,gq, or $q\bar{q}$.

This paper describes a high-statistics study of three-jet production using the Collider Detector at Fermilab (CDF). Emphasis is placed on the study of those variables which explore the nature of the singularities described above. This study represents an improvement

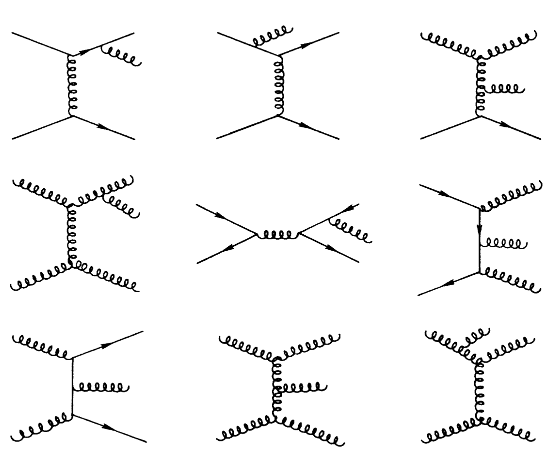

FIG. 1. Some of the diagrams contributing to three-jet final states in $p\bar{p}$ collisions.

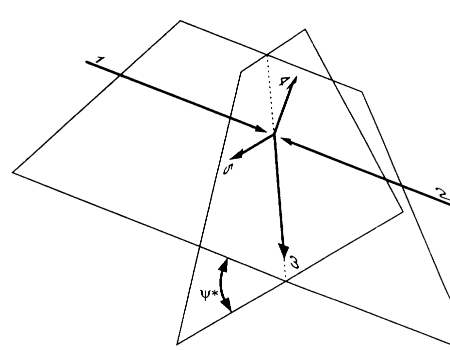

FIG. 2. Illustration of the variable ψ^*. ψ^* is the angle between the plane containing the beam line and the highest-energy jet in the c.m.s. frame, and the next two highest-energy jets. As $\psi^* \rightarrow 0°$ or 180°, the contribution of initial-state radiation from incoming partons increases the rate.

over previous results reported by experiments at the CERN S$p\bar{p}$S collider [1,2] in the statistics available, and with the higher jet energies in the accessible range of kinematics.

II. DETECTOR

The data used for this analysis consists of an exposure of 4.2 pb^{-1} using the Collider Detector at Fermilab (CDF) at a center-of-mass energy $\sqrt{s}=1.8$ TeV. The CDF detector, shown in Fig. 3, has been described in detail elsewhere [3]. Here we note detector elements relevant for the present analysis. The calorimeters consist of projective towers covering the complete azimuth and the pseudorapidity range $-4.2<\eta<4.2$ where η is related to the polar angle θ by the relation $\eta=-\ln[\tan(\theta/2)]$. The projective tower geometry points back to the center of the detector. The event vertex position, however, can be shifted along the beam line and has an rms width of approximately 30 cm. We will refer to detector pseudorapidity η_d for an origin chosen at the geometric center of the detector, to avoid confusion with physical pseudorapidity η which takes the event vertex as the origin.

In the central region ($|\eta_d|<1.1$), an 18 radiation length Pb-scintillator electromagnetic compartment is followed by a minimum of four absorbtion lengths of Fe-scintillator hadronic calorimetry. The tower segmentation is 15° in ϕ and 0.1 in η_d. The towers are read out by a pair of phototubes which bracket the towers in azimuth and can be used to provide a rough ϕ centroid for isolated tracks. The plug ($1.1<|\eta_d|<2.4$) and forward ($2.4<|\eta_d|<4.2$) calorimeters contain alternating layers of lead (steel) radiators and gas proportional tubes for the electromagnetic (hadronic) compartment. Segmentation is roughly 5° in ϕ and 0.1 in η_d. Tracking is performed inside a 1.4-T magnetic field using a central tracking chamber (CTC) and the event vertex is reconstructed using a series of time-projection chambers that surround the beam pipe.

Events were required to pass a hardware trigger consisting of a coincidence of at least one particle in each of the upstream and downstream scintillation counters ($3.2<|\eta_d|<5.9$) in conjunction with a minimum total transverse energy summed over calorimeter towers. For the trigger, individual towers were ganged into "trigger towers" of size $\Delta\phi=15°$, $\Delta\eta_d=0.2$. Electromagnetic and hadronic compartments were summed separately and only trigger towers with at least 1-GeV transverse energy were included in the sum. The threshold for the total (EM+hadron) transverse-energy trigger was 120 GeV. A total of 466 285 events were taken with this trigger.

In addition to the summed E_t trigger used for this analysis, CDF recorded events that passed a cluster-based "jet" trigger which required a contiguous set of trigger towers, each with a minimum transverse energy of 1 GeV per tower and E_t summed over towers above a given threshold. Cluster thresholds of 20, 40, and 60 GeV were used with prescale factors of 300, 30, and 1, respectively. For this analysis, events from these triggers were used to check the detector response to jets as a function of E_t and η_d.

III. JET CLUSTERING ALGORITHM

The CDF jet clustering algorithm uses a cone of a fixed radius to define a jet. In this sense, it is closely related to the algorithm used by the UA1 experiment [4] and corre-

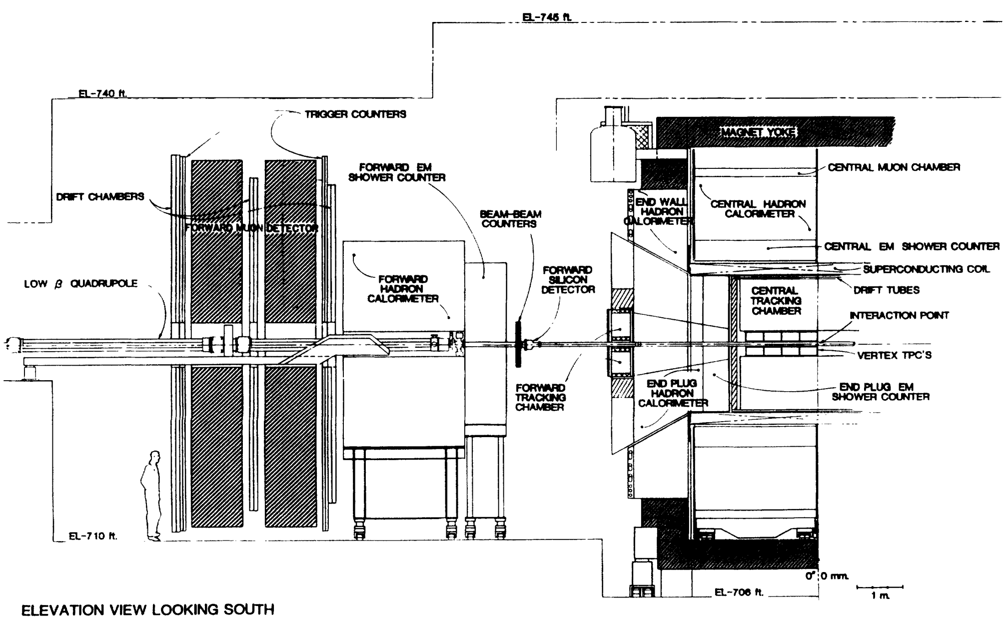

FIG. 3. Schematic of the CDF detector. Most relevant to this analysis are the calorimeter systems which span the region of pseudorapidity $-4.2\le\eta\le4.2$. The central tracking chamber (CTC) is used to perform *in situ* calibration checks of the central calorimeter, and also measure jet fragmentation properties.

sponds closely to the definitions used in calculating QCD cross section [5–7]. In addition, studies have shown that the cone definition produces a cleaner separation in the η-ϕ metric than other definitions (e.g., nearest-neighbor algorithms) [8].

The jet-finding algorithm begins by creating a list of towers above a fixed E_t threshold to be used as seeds for the jet finder. This threshold is set to 1.0 GeV. In the plug and forward calorimeter regions, towers are grouped together in sets of three in ϕ, spanning 15° to correspond to the central segmentation. Preclusters are formed from an unbroken chain of contiguous seed towers with a continuously decreasing tower E_t. If a tower is outside a window of 7×7 towers surrounding the seed, it is used to form a new precluster. These preclusters are used as a starting point for cone clustering.

The preclusters then are grown into clusters using the true tower segmentation (i.e., no ganging). First, the E_t weighted centroid of the precluster is found and a cone in η-ϕ space of radius R is formed around the centroid. For this analysis, $R=0.7$. Then, all towers with an E_t of at least 100 MeV are incorporated into the cluster. A tower is included in a cluster if its centroid is inside the cone [9]; otherwise it is excluded. A new cluster center is calculated from the set of towers within the clustering cone, again using an E_t weighted centroid, and a new cone is drawn about this position. The process of recomputing a centroid and finding new or deleting old towers is iterated until the tower list remains unchanged.

The choice of $R=0.7$ is based partly on the distribution of energy flow with respect to the jet axis in events dominated by two jets. Figure 4 shows this plot for dijet events where the leading jets have values of E_t of approximately 40 GeV. There is a rather broad minimum between the lead jet ($\phi=0$) and recoil ($\phi=\pi$) directions. It is clear that cone sizes as small as 0.4, or as large as 1.0 may be sensible. Other studies, for example by UA2 [10], give evidence that a range of $0.4<R<1.0$ yield good resolution. In this context, the choice of $R=0.7$ is somewhat arbitrary, but does fall in the middle of a sensible range of cone sizes. It is more important, however, that the QCD predictions used for comparisons reflect this jet size, and that the separation in η-ϕ be understood.

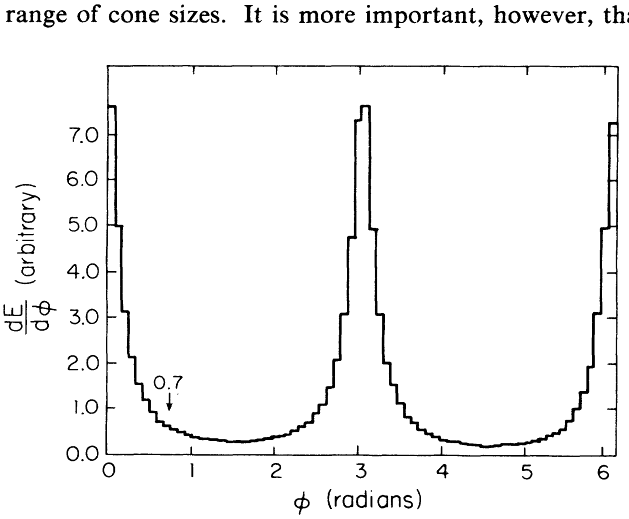

FIG. 4. Azimuthal energy flow with respect to the jet axis in dijet events. Note that cone sizes from $R=0.4$ to $R=1.0$ can contain most of the energy.

For multijet studies, it is important to handle properly conditions where two clusters overlap, particularly for final-state gluon emission where the gluon can merge into the jet. There are four possible overlap conditions. The first two cases are trivially handled. If two clusters are distinct, they are left alone. If one cluster is completely contained in another, the smaller of the two is dropped. If the towers have some finite overlap, then an overlap fraction is computed as the sum of the E_t of the common towers divided by the E_t of the smaller cluster. If the fraction is above a cutoff (0.75) then the two clusters are combined. If the fraction is less than the cut, the clusters are kept intact. In this case, each tower in the overlap region is assigned to the cluster closest in η-ϕ space. After the clusters are uniquely assigned to towers, the centroids are recomputed. As with the original cluster finding, the process of centroid computation and tower reshuffling is iterative, and ends when the tower lists remain fixed.

From the towers associated with the cluster, the quantities (p_x,p_y,p_z,E) are calculated. The electromagnetic and hadronic compartments of each tower are assigned massless four-vectors with magnitude equal to the energy deposited in the tower and with the direction defined by a unit vector pointing from the event origin to the center of the face of the calorimeter tower (calculated at the depth that corresponds to shower maximum). E is the scalar sum of tower energies; p_x is the sum of $p_{x,i}$ where i is the tower index. Other quantities, such as E_t can then be determined. For example, $E_t \equiv E\sin\theta = E\sqrt{p_x^2+p_y^2}/\sqrt{p_x^2+p_y^2+p_z^2}$.

Because the z vertex position is spread out along the beam line, forming a Gaussian with a width of approximately 30 cm, it is necessary to correct the pseudorapidity of all jets from η_d to η. This shift implies a small correction of energy to take into account the incidence angle of the jets on the face of the calorimeter.

For studies of multijet events, it is important to understand the separation of jets in the η-ϕ metric. One of the desirable characteristics of a jet algorithm is the ability to produce cleanly separated jets. The angular resolution of the jet finder was studied by taking pairs of events, each with two cleanly identified jets with $E_t \geq 25$ GeV, and embedding jets from one event into a second event and reapplying the jet-finding algorithm. Figure 5 shows the probability that clusters from two individual events will be merged as a function of the η-ϕ separation between the clusters. For a cone size of $R=0.7$, the merging probability is 25% for any η-ϕ separation of 0.85. The slope is quite steep, indicating that this merging radius is relatively stable.

IV. JET ENERGY CORRECTIONS

The transverse energies and momenta in the above definition (which will henceforth be termed "uncorrected energy") depend only on the energy deposition observed in the calorimeter. These uncorrected quantities differ from the true partonic values for a variety of reasons. Some of these are the result of limitations in detector per-

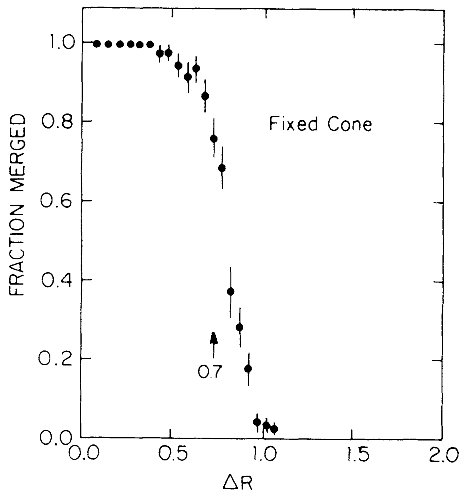

FIG. 5. Fraction of jets in event mixing studies found merged into a single jet as a function of separation in $R \equiv \sqrt{\Delta\eta^2 + \Delta\phi^2}$. Note the sharp cutoff in the merging near the cone radius used in the jet definition ($R = 0.7$). The minimum cluster E_t for jets in this plot was 25 GeV.

formance.

(i) The calorimeter response to low-energy charged pions exhibits a nonlinearity for momenta below 10 GeV.

(ii) Charged particles with transverse momenta below ~400 MeV bend sufficiently in the magnetic field that they do not reach the calorimeter. At slightly higher transverse momenta, the magnetic field can bend particles outside the clustering cone.

(iii) Particles that shower in boundary regions of the calorimeter (the ϕ boundaries between modules in the central calorimeter and η_d boundaries between the two halves of the central calorimeter, between the central and plug calorimeters and between the plug and forward calorimeters) will, on average, have a smaller energy reported than for regions of uniform response.

Others result from fundamental elements of the physics process.

(iv) Energy not associated with the hard-scattering process (the so-called "underlying event") will be collected within the clustering cone.

(v) Transverse spreading of the jet due to fragmentation effects will cause particles to be lost outside the clustering cone.

(vi) Energy in neutrinos and muons, which deposit either zero or some small fraction of their energy in the calorimeter.

A correction function which takes into account these effects is generated and applied to jets in the data sample. This function is a map of the detector response for different energies and values of η_d.

The procedure for generating the response map has three parts. The first is the determination of the response of the central calorimeter to jets. This is facilitated by the use of the central tracking chamber (CTC) to measure jet-fragmentation properties [11], and to provide an *in situ* measurement of response to low-momentum ($p < 10$ GeV) charged particles.

Second, the response in the central calorimeter is then extended into other regions of the detector, where charged-particle momentum determination is not available, using a technique where the E_t of jets in the central calorimeter is required to balance the E_t of jets in the plug and forward calorimeters. Finally, corrections are determined for energy escaping the jet cone, and being added by the underlying event.

A. Central jet response

The response of the central calorimeter to pions has been measured both in test beams and *in situ*. Figure 6 shows the measured calorimeter response to charged hadrons as a function of incident momentum for particles hitting the center of a calorimeter tower. The figure also indicates the size of the systematic error associated with this measurement. Note that the measured response deviates substantially from linearity for low incident energy.

Because the calorimeter response to charged hadrons is nonlinear, the observed jet energy is a function not only of the incident parton energy but also of the momentum spectrum of the particles produced in the fragmentation process. It is important that Monte Carlo events used in jet studies reproduce the observed fragmentation properly. We have chosen to use an exact matrix-element calculation for all QCD comparisons in this paper [12]. It was necessary to adjust parameters in the event generator to reproduce the observed jet-fragmentation distributions.

The calorimeter response and jet-fragmentation properities are measured in the central tracking chamber (CTC). The CTC has a track-reconstruction efficiency of better than 80% in the core of jets for values of E_t up to 100 GeV. The efficiency for reconstructing isolated tracks is better than 98%. An event generator based on the Field-Feynman [13,14] parametrization of fragmentation is tuned to reproduce the observed longitudinal and transverse fragmentation properties observed in the CTC.

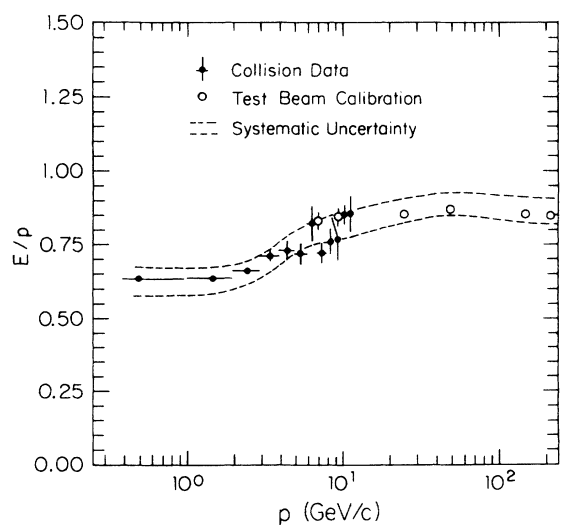

FIG. 6. CDF central calorimeter response (E/p) to pions as a function of incident momentum. The high-energy data come from test beam measurements, and the low-energy data (≤ 12 GeV) comes from isolated tracks in minimum-bias events.

A check of this tuning is shown in Fig. 7 where the charged particle multiplicity observed inside the jet cone is compared to the same quantity as reproduced by the event generator and detector simulation.

After the jet fragmentation properties are measured, the jet responses were determined for the central calorimeter. To do this, dijet events were generated with an approximately flat p_t spectrum ($10 \le p_t \le 700$ GeV), and a flat η spectrum. The dijet events were then given a transverse boost ("k_t" kick) to simulate the effects of soft-gluon radiation. The k_t distribution was tuned to agree with the observed distribution in CDF data. The partons were fragmented using the tuned Field-Feynman parametrization [13,14]. The generation and simulation included particles from the underlying event associated with the soft spectator partons. The simulated jets were reconstructed using the standard CDF algorithm and cone size $R = 0.7$. The uncorrected cluster p_t was then compared to the sum of the p_t of all generated particles lying in a cone of $R = 0.7$ centered about the measured jet axis, and originating from the primary partons. Particle trajectories were calculated according to their initial momenta rather than their impact point on the calorimeter. A quadratic spline fit was used to parametrize the mean jet response as a function of E_t.

B. Pseudorapidity dependence

To measure the η_d dependence of the jet response, dijet events with at least one central jet were selected, and the relative response was extracted by comparing the p_t of the central jet with the p_t of the other jet, as a function of the η_d position of the other jet.

Dijet events were selected from the "jet" triggers by requiring at least two jets with uncorrected p_t above 15 GeV. To avoid bias from the on-line trigger requirement, the sum of the transverse momenta of the two leading jets was required to exceed twice the value of the single-jet trigger threshold. At least one of the leading two jets was required to lie within the central detector ($0.15 \le |\eta_d| \le 0.9$).

Figure 8 plots the average p_t imbalance fraction for these events as a function of detector η. The imbalance is defined as the missing p_t from the jets divided by their average p_t, and directly measures the ratio of the effective jet energy scale of the central detector to the probed region. To generate this plot, a central jet was required with $0.15 \le |\eta_d| \le 0.9$; hence, this figure represents the averaged response of the recoil jet in different regions of η_d. The peaks near $\eta_d = \pm 1$, and ± 2.2 come from loss of response due to boundaries between calorimeters. The response is parametrized both as a function of η_d and of jet E_t, where 36 parameters are sufficient to describe the entire map. This map is shown in Fig. 9 for different slices of jet p_t. In Fig. 8, the result of applying the correction map to the dijet balancing data demonstrates that the map indeed takes out the known η_d dependence. The jet resolution (rms) as a function of η_d in slices of jet E_t is shown in Fig. 10. Note the degradation in response in the η_d boundary regions. The data are limited to $|\eta_d| \le 2.4$ due to kinematic effects. This limitation does not pose a problem for the analysis as $\ge 97\%$ of jets in the three-jet sample are in the region $|\eta_d| \le 2.4$.

C. Underlying event and clustering corrections

The underlying event is the ambient energy produced in hadron collisions associated with the soft interactions of spectator partons. The energy from the underlying

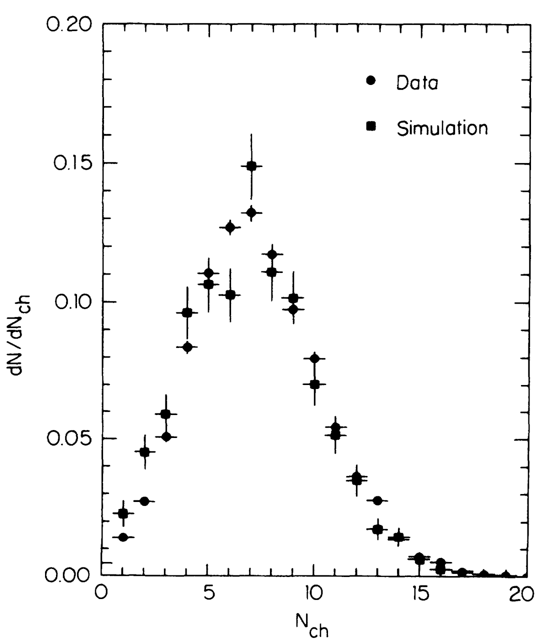

FIG. 7. The charged-particle multiplicity observed inside the jet clustering radius (R) in the CDF data and as reproduced by the event generator and detector simulation.

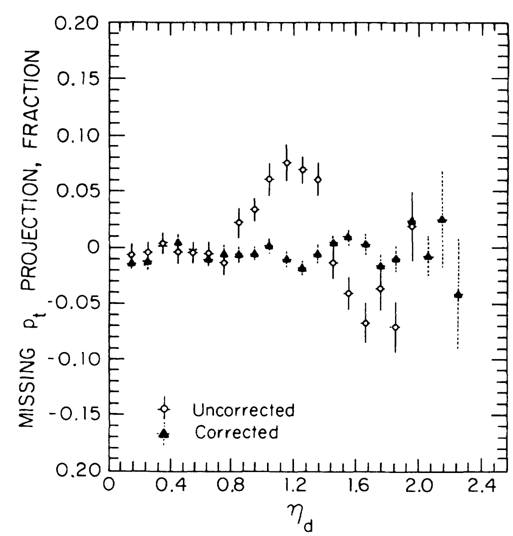

FIG. 8. The fractional p_t imbalance of two-jet events where one jet was taken in the central region ($0.15 \le |\eta_d| \le 0.9$), and the recoil jet was allowed to fall in any region of detector pseudorapidity (defined in the text). The uncorrected jet response (circles) shows the effects of boundary regions between calorimeters. The effect of the corrections (triangles) is to make the events balance in p_t.

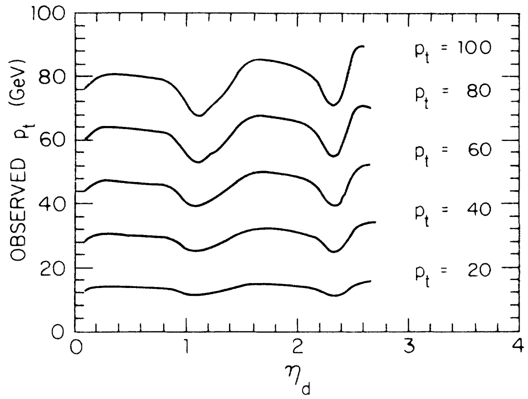

FIG. 9. Parametrization of the jet response map as a function of detector pseudorapidity η_d for different slices of jet p_t. Note the variations in response reflected in the p_t imbalance map (Fig. 8).

event will increase the effective energy found in the jet cone, yet will not be truly associated with the hard-scattering process. The energy that falls out of the clustering cone is associated with fragmentation effects and gluon radiation. In this analysis, the underlying event energy was subtracted, and the average energy falling outside the cone was added to the jet energy. We studied both effects using data and the Monte Carlo model described above. We have found that both effects are roughly independent of leading jet E_t over the range of interest, and small compared to the typical jet energies used in this analysis. The combined correction for both of these effects represents a constant value of 500 MeV which is added to the jet energy.

D. Uncertainties in energy scale

The dominant systematic uncertainty in the central jet energy scale results from the uncertainty in the single-pion response when convoluted with the jet fragmentation function [15]. The uncertainty in single-pion response is indicated by the dashed lines in Fig. 6. The uncertainty in the central energy scale for jets can be expressed as a 40% E_t-independent term, plus an E_t-dependent term which can rise as high as 7% at low E_t (≈ 25 GeV). The E_t dependent part of the uncertainty results from both the uncertainties in the jet fragmentation, and in the shape of the low energy part of the single pion response. The E_t independent part of the uncertainty comes from two main sources. The first is our ability to properly model the variation of the single-pion response over the face of a calorimeter tower. The second is from the agreement of test beam and *in situ* calibrations for pions of the same momentum, which provides a check of the reproducibility of the energy scale calibration.

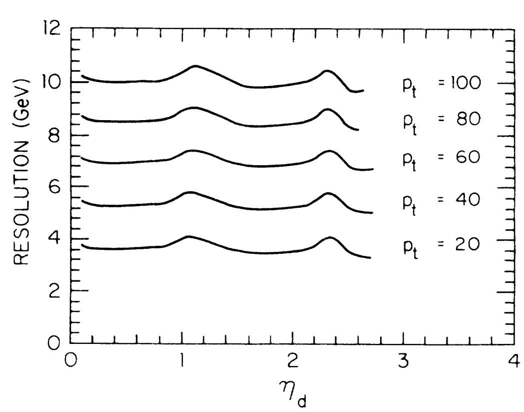

FIG. 10. Parametrization of the rms jet resolution as a function of detector pseudorapidity η_d for different slices of jet p_t.

The extrapolation into the forward-backward regions of the detector gives an uncertainty which can be as large as 5% in the plug-central boundary region. By adding all sources in quadrature, one obtains an uncertainty which can be as large as 10% for jets with $|\eta_d| \approx 1.3$ and $E_t \approx 25$ GeV, or as low as 4% for jets with $0.1 \leq |\eta_d| \leq 0.7$ and $E_t \geq 250$ GeV. It should be noted that most of the jets used in this analysis are high-E_t jets in the central region, so 4–6 % is representative of the bulk of the data.

V. ANALYSIS

Events are selected from the summed E_t triggers with a threshold of 120 GeV. Three-jet events are selected by requiring at least three jet clusters in the region $|\eta_d| < 3.5$ with $E_t > 10$ GeV (uncorrected—this corresponds to a parton E_t of approximately 15 GeV), each separated by a minimum distance $\Delta R \geq 0.85$ in η-ϕ space. If four or more jets are present, we form quantities from the three with the highest E_t. To ensure good containment of the energy, we require that the primary event vertex be on the beam line within 60 cm of the center of the detector. This cut reduced the event sample by 5%.

For each event, the corrected four-momenta of the leading three jets are boosted to the three-jet center-of-mass frame. The four-momenta are assumed to be those of the final-state partons. Following the convention of Refs. [1] and [16], the initial-state partons are labeled 1 and 2, 1 being the highest-energy parton in the lab frame, and the final-state partons are labeled 3 through 5 in order of decreasing energy in the three-jet center-of-mass system. The convention of Collins and Soper [17] is used to define the beam line in this frame.

In general, nine parameters are required to describe the kinematics of a three-parton system. Three give the boost from the lab into the three-jet center-of-mass system. The largest of these is typically the boost of the system along the beam line, z_{boost}, defined by the expression

$$z_{\text{boost}} = \frac{1}{2} \ln \frac{x_1}{x_2} , \tag{1}$$

where x_1 and x_2 are the momentum fractions of the proton and antiproton carried by the partons participating in the hard scatter. The boosts in the transverse plane (x,y) are typically small (of order a few GeV).

The other six parameters specify the properties of the three jets in their center-of-mass frame. Three of these describe the angular orientation and three specify how the total center-of-mass energy is shared among the jets.

The three angles, which are related to the Euler angles used to specify the orientation of a rigid body, are θ^*, ψ^*, and ϕ^*. θ^* is the angle between parton 3 and the beam line. ψ^* (described in the Introduction, Fig. 2) is the angle between the plane of the three final-state partons and the plane described by parton 1 and parton 3. ϕ^* is the azimuthal angle of parton 3. Since there is no beam polarization at the Tevatron, the dependence on ϕ^* is trivial, and can be integrated over.

M_{3j} is the invariant mass or three-jet c.m.s. energy of the three partons, and is equivalent to the subprocess energy if there are no more than three jets. The final-state parton energy fractions are x_3, x_4, and x_5:

$$x_i = \frac{2E_i}{M_{3j}} . \qquad (2)$$

x_3 varies between $\frac{2}{3}$ and 1, x_4 between $\frac{1}{2}$ and 1, and x_5 between 0 and $\frac{2}{3}$. The extremes correspond to the limit of a symmetric three-jet event for $x_3 = \frac{2}{3}$ and a two-jet event ($x_3 = 1$). Specifying x_3 and x_4 fixes all three energy fractions since $x_3 + x_4 + x_5 = 2$. Hence x_5 is not an independent variable. Four variables therefore are sufficient to describe the nontrivial c.m.s. behavior of the three-parton final states.

Based on an analysis of x_3, x_4, ψ^* and $\cos\theta^*$ for Monte Carlo–generated three-jet events, a set of kinematic cuts were developed to ensure that the acceptance be uniform for the data set to within approximately 15% for all variables. With the exception of the regions $x_3 \leq 0.72$ and $x_4 \leq 0.6$, the acceptances vary less than 7%. Nearly all of the data are contained in the region with acceptance variations less than 7%. The Monte Carlo generators included both phase space and QCD matrix elements, giving similar results for the acceptances. In both cases, the partons are fragmented and the resulting hadrons are passed through a detailed detector simulation and then analyzed using the same procedure as for the data.

The trigger requirement of a summed E_t of at least 120 GeV can seriously bias the jet distributions unless appropriate kinematic cuts are applied. We therefore have required for most of our analysis that the three-jet events satisfy the conditions $M_{3J} > 250$ GeV, $|\cos(\theta^*)| < 0.6$, and $30° < \psi^* < 150°$. It is possible to extend the ψ^* or $\cos(\theta^*)$ range of the analysis by raising the minimum value of M_{3J}. In addition, to ensure that all events contain well-separated jets, we require $x_1 < 0.9$. A total of 4826 events remains after these cuts.

VI. QCD COMPARISON

The $\bar{p}p$ c.m.s. energy and statistics available at CDF have allowed a more detailed examination of QCD dynamics for multijet systems than was possible at lower $\bar{p}p$ c.m.s. energies (S$\bar{p}p$S). At the present time calculations are not available beyond the tree level for $2 \rightarrow 3$ processes. Current theoretical work on the calculation of the inclusive jet cross section at order α_s^3 [7,6] may eventually lead to a more complete calculation of three-jet final states in hadron-hadron collisions. The tree-level matrix elements, however, give faithful results providing they are evaluated for parton configurations far away from the dominant singularities (i.e., collinear or infrared) [18].

In the standard formalism, the cross section can be written in terms of the subprocess cross sections as

$$d\sigma_n = \sum_n \int dx_1\, dx_2\, F_1(x_1, Q^2) F_2(x_2, Q^2) d\hat{\sigma}_n , \qquad (3)$$

where F_1 and F_2 are the parton distribution functions for the proton and antiproton and $\hat{\sigma}_n$ is the subprocess cross section. For the three-parton final state, tree-level calculations have existed for some time [16]. These matrix elements, employed in the QCD predictions presented here, have divergences associated with soft-gluon emission (infrared) and collinear configurations. These singularities are avoided by the requirements placed on the minimum parton separation and E_t in evaluating the matrix elements.

Two relevant subprocesses examined here involve all gluons or two quarks and three gluons. The differences among the subprocesses reflect the different dynamics associated with the three-gluon vertex and the quark-gluon vertex. In a compact notation [19], the tree-level expression for the square of the matrix elements for the subprocess $gg \rightarrow ggg$ is

$$|M(g_1, \ldots, g_5)|^2 = 2g_s^6 N^3 (N^2 - 1) \times \sum_{i>j} s_{ij}^4 \sum \frac{1}{s_{12}s_{23}s_{34}s_{45}s_{51}} . \qquad (4)$$

Here N denotes the number of colors, and s_{ij} is the dot product $p_i \cdot p_j$ between the four-momenta of partons i and j. The second sum runs over nonidentical permutations of the indices $1, \ldots, 5$, where $i \neq j$ (e.g., $s_{12}s_{23}s_{34}s_{45}s_{51}$ is identical to $s_{51}s_{12}s_{23}s_{34}s_{45}$). In contrast, the corresponding expression for processes involving a q and $\bar{q}$ in either initial or final states is [19]

$$|M(q,\bar{q},g_1,g_2,g_3)|^2 = 2g_s^6 N^2 (N^2 - 1) \times \sum_i (s_{qi}^3 s_{\bar{q}i} + s_{qi} s_{\bar{q}i}^3) \times \sum_{(1,2,3)} \frac{1}{s_{q\bar{q}} s_{q1} s_{12} s_{23} s_{3\bar{q}}} , \qquad (5)$$

where i is the index for gluons. Note the difference in the term in the first sum. This reflects the difference in the spins and couplings of gluons and quarks. In addition, most of the differences associated with $q\bar{q}$, gg, and gq initial states in the distributions presented here can be understood in the naive interpretation that gluons radiate more than quarks.

In order to determine the cross sections for the variables of interest, the Eichten-Hinchliffe-Lane-Quigg (EHLQ) parton distribution functions, set 1 [20] were employed. Also, the set of Diemoz, Ferroni, Longo, and Martinelli [21] were employed to study the sensitivity of choice of parton distribution function. Equation (3) was used with the matrix elements in Ref. [16]. Partons were generated and were fragmented using a Field-Feynman fragmentation function which was tuned, as described earlier, to reproduce both the longitudinal and transverse distributions of charged energy flow observed in CDF data. In addition, the underlying event was tuned to reproduce the energy flow seen in jet events.

The parton level requirements were placed on the generation of matrix elements to avoid divergences in the cross section. The cuts employed in the generation of events were (1) $E_t >$ 15.5 GeV (all three partons), (2) $\sqrt{\hat{s}} >$ 200 GeV, (3) $|\eta| <$ 4.0, (4) ΔR separation > 0.70.

After fragmentation and the detector simulation, the events were subjected to the same cuts as the data. Given these cuts, acceptances in all variables studied (x_3, x_4, ψ^*, and $\cos\theta^*$) were flat to within 7% over the ranges reported except for $x_3 \leq 0.7$ and $x_4 \leq 0.6$ where acceptances could vary by up to 15%.

The three-jet cross section predicted using the tree-level event generation and the selection criteria imposed on the data is 1.8±0.9 nb. The uncertainty results from the choice of parton distribution function (±0.3 nb), and from the choice of renormalization scale used for evaluating α_s and the evolution of the parton distribution functions (±0.9 nb). The large uncertainty in the theoretical cross section is due to terms of order α_s^3 in the tree-level calculation. From the data, we determined a cross section of 1.2±0.02 (stat)±0.6 (syst) nb for three-jet production passing the selection criteria described above. The systematic uncertainty was obtained by varying the M_{3j} cut by 10%, in accord with the upper bound in the energy scale uncertainty discussed in Sec. IV D. There is an additional uncertainty in the integrated luminosity (7%) [22] which is negligible compared to the uncertainty from energy scale. Within the large uncertainties, there is agreement between the theoretical and measured cross sections.

With the parton level cuts described above, it is possible to break down the predicted three-jet cross section in terms of the contributions from different subprocesses. Following are the contributions from subprocesses which contribute more than 4% to the total cross section: (1) $gg \to ggg$ 36%, (2) $qg \to qgg$ 22%, (3) $g\bar{q} \to gg\bar{q}$ 22%, (4) $gg \to q_i\bar{q}_i g$ 5%, (5) $q_i\bar{q}_j \to gq_i\bar{q}_j$ 4%, and (6) $q_i\bar{q}_i \to gq_i\bar{q}_i$ 4%. Here i,j are flavor indices for the quarks. These numbers are based on cross sections using the EHLQ parton distribution functions [20].

The variables x_3 and x_4 are plotted together in the Dalitz plot in Fig. 11. Phase space would populate the triangle uniformly. Deviations from a uniform distribution show the effect of QCD dynamics. To be specific, one expects enhancements in the cross section near the upper right-hand edge ($x_3 \approx 0.9, x_4 \approx 0.9$) of the plot due to the enhancement of the cross section when a third jet is very soft.

Taking the three-jet Dalitz plot and projecting on either axis, the distributions of the variables x_3 and x_4 can be obtained. Figure 12 shows the comparison of the measured distribution of x_3 with the full (i.e., including all subprocesses) QCD calculation and with the predictions for subprocess involving $q\bar{q}$ in the initial state. In addition, the predictions of a constant matrix element (phase space) is also indicated. The data clearly prefer the full QCD prediction over processes involving only $q\bar{q}$ in the initial state, and over phase space. Although not plotted, the shapes of the x_3 from gg and gq initial states are nearly identical. Figure 13 shows a similar comparison of data to the tree-level predictions for x_4. As with x_3, the QCD predictions agree with data, and the shape from the $q\bar{q}$ initiated subprocesses is distinctly different. The differences in the x_3 and x_4 distributions for $q\bar{q}$ initial states and full QCD, which is dominated by gg and gq initial states at these energies, is consistent with the naive view that gluons radiate more than quarks and hence give

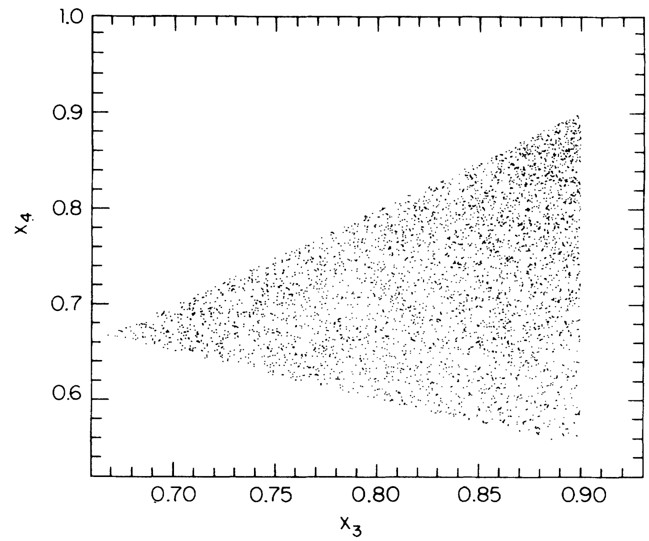

FIG. 11. Dalitz plot of x_4 vs x_3 for the data set. A constant matrix element (phase space) would generate a uniform distribution inside this plot. An enhancement in the upper right-hand corner is expected due to infrared singularities in QCD.

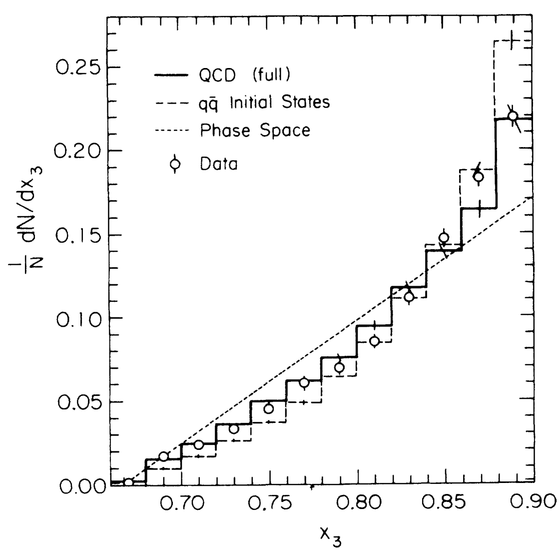

FIG. 12. The distribution of x_3 in the final event sample. Errors are statistical only. The predictions from a tree-level QCD calculation are shown as the solid line. In addition, the predictions of phase space, and from $q\bar{q}$ initial states are also shown. Error bars on the histograms are the approximate size of the statistical error from the Monte Carlo generation of the theory curves. The data show reasonable agreement with the QCD prediction; however, they are incompatible as arising from either phase space, or as originating from only $q\bar{q}$ subprocesses.

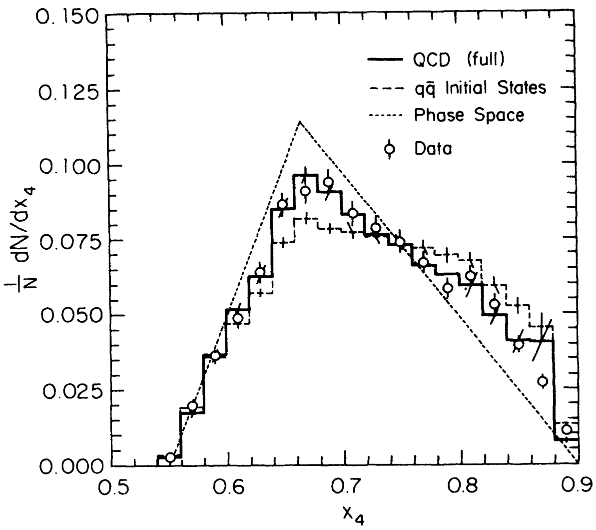

FIG. 13. The distribution of the next-to-leading jet energy fraction, x_4 shown along with the predictions of the QCD tree-level calculation (solid), phase space, and from subprocesses involving only $q\bar{q}$ in the initial state. As with x_3, the data are in good agreement with the full QCD calculation, and consistent with the expected small contribution from subprocesses involving $q\bar{q}$ in the initial state.

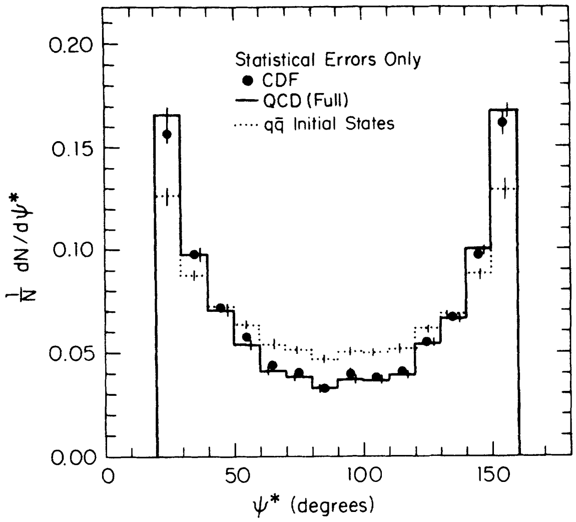

FIG. 14. The distribution of ψ^*, the angle between the plane containing the beam and the leading jet and the plane containing the 2 nonleading jets in the c.m.s. frame. The predictions and data exhibit a characteristic peaking associated with *bremsstrahlung* from initial-state partons at $\psi \approx 180°$ and 0°. The peaking is more pronounced for the full QCD prediction than for the case involving only two quarks in the initial state.

rise to distributions which appear more like phase space. The χ^2 for x_3 is 16 (11 DOF) and 13 (17 DOF) for x_4 for the full QCD prediction.

Figures 14 and 15 show the results for ψ^* and $\cos\theta^*$ respectively compared with tree-level predictions. The peaking of ψ^* in the forward/backward ($\psi^* \approx 0°$ and 180°) regions is associated with increasing cross section for a third jet to be found close to the axis of the incoming partons. As above, the difference between full QCD and the predictions for $q\bar{q}$ subprocesses is consistent with the naive interpretation that gluons radiate more than quarks.

The $\cos\theta^*$ distribution shows the forward peaking expected by processes dominated by $\hat{t}$-channel exchange of vector particles, with an observable difference between the full QCD calculation and $q\bar{q}$ initiated subprocesses. In this case the difference associated with the $q\bar{q}$ states can be attributed to the different mixture of s- and t-channel-exchange processes.

We have fit the fraction of events arising from the $q\bar{q}$ initial states as a free parameter. A one-parameter fit is sensible inasmuch as the qg- and gg-initiated processes all have similar shape distributions and $q\bar{q}$ distributions are different; this is true for all four variables. $\cos\theta^*$, ψ^*, x_3, and x_4 have been fit for the $q\bar{q}$ fraction in a combined fit. χ^2 values for all four distributions are summed together to derive an overall χ^2. In all cases, the statistical error in the Monte Carlo distributions are included in the χ^2. The fit for the full QCD calculation using the EHLQ set-1 parton distribution functions [20] gives a χ^2 of 75 for 62 DOF. For the cuts imposed on the data, one expects a $q\bar{q}$ fraction of 0.11 ± 0.04. The uncertainty on the $q\bar{q}$ fraction was derived by using Diemoz-Ferroni-Longo-Martinelli (DFLM) [21] parton distribution function, which gave a 4% higher result than EHLQ. We took this difference to be representative of the typical variation seen with different parton distribution functions, and quote it as a symmetric uncertainty about the EHLQ value. For any given subprocess, the actual distributions are very insensitive to choice of parton distribution function. When the $q\bar{q}$ fraction is fitted as a free parameter for the data, a fraction of $0.03+0.04-0.03$ is derived. The best fit has a χ^2 of 73 for 62 DOF, and is consistent with the QCD prediction.

In selecting the events, the number of jets with E_t greater than 15 GeV was required to be greater than or

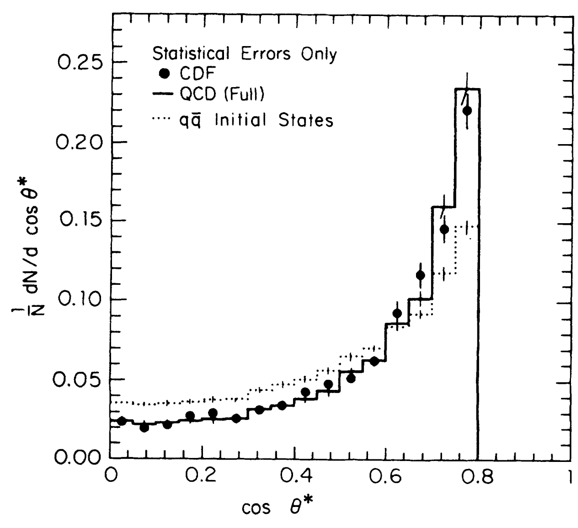

FIG. 15. The c.m.s. angular distribution of the leading jet with respect to the beam axis, $\cos\theta^*$. As with the other distributions, the data are consistent with QCD and consistent with a small overall contribution from $q\bar{q}$ initiated subprocesses.

equal to 3. The number of events with more than three jets above this threshold is 2235 (out of 4826). It is appropriate to compare the entire sample to tree-level graphs involving three jets in the final state, rather than to attempt to define an exclusive three-jet cross section (i.e., three and only three jets) as such a cross section is difficult to calculate in perturbation theory. For example, the cross section for a 0 GeV fourth parton in a 4 parton tree-level calculation is infinite due to infrared divergences. Also, it is impossible experimentally to obtain a sample of three and only three jets due to the presence of other energy in the event. Nonetheless, we examined the effect of a cut on the fourth jet in the sample. This was done by comparing the 2235 events with a fourth jet above 15 GeV E_t with the remaining sample. For the variables examined, variations between the two subsets were typically at the level of the statistical uncertainties. The result is consistent with the results of a 4-jet Monte Carlo study.

VII. CONCLUSION

We have studied the production of three-jet final states in $p\bar{p}$ collisions at $\sqrt{s}=1.8$ TeV with the CDF detector. For a set of cuts designed to isolate kinematic regions where acceptances are flat to within 7% we have found a cross section that is consistent with tree-level predictions. The fractional energies carried by the leading two jets in the three-jet c.m.s. system, x_3 and x_4, are consistent with the predictions of the tree-level QCD calculations. The shapes of the data are consistent with a small numerical contribution originating from subprocesses with $q\bar{q}$ in the initial state.

The c.m.s. angle between the leading jet and the beam line, $\cos\theta^*$, is peaked in the forward direction and is consistent with the tree-level calculations. The ψ^* distribution is also consistent with the tree-level calculations. The small fraction of events resulting from $q\bar{q}$-initiated subprocesses determined from a fit to all four distributions are consistent with theoretical expectations. These conclusions are unaffected by cuts which isolate events containing a fourth jet.

ACKNOWLEDGMENTS

We thank the Fermilab Accelerator Division for their exceptional performance in the operation of the Tevatron and the Antiproton Source. This work was supported in part by the Department of Energy, the National Science Foundation, Istituto Nazionale di Fisica Nucleare, the Ministry of Science, Culture and Education of Japan, and the A. P. Sloan Foundation.

[1] G. Arnison et al., Phys. Lett. **148B**, 494 (1985).
[2] J. Appel et al., Z. Phys. C **30**, 341 (1986).
[3] CDF collaboration, F. Abe et al., Nucl. Instrum. Methods A **271**, 387 (1988).
[4] G. Arnison et al., Phys. Lett. **132B**, 214 (1983).
[5] G. Sterman and S. Weinberg, Phys. Rev. Lett. **39**, 1436 (1977).
[6] F. Aversa et al., Phys. Lett. B **210**, 225 (1988).
[7] S. Ellis, Z. Kunszt, and D. Soper, Phys. Rev. Lett. **62**, 2188 (1989).
[8] John Huth, in *Calorimetry for the Superconducting Super-Collider*, Proceedings of the Workshop, Tuscaloosa, Alabama, 1989, edited by R. Donaldson and G. Gilchriese (World Scientific, Singapore, 1990), pp. 27–58.
[9] The tower centroid is calculated from the E_t weighted centroid of the EM and hadronic compartments. Because the z vertex may be displaced from the geometric center of the detector, a vector drawn from the event vertex to the expected position of shower maximum in a tower will fall in different values of pseudorapidity. These positions, weighted by the E_t in each compartment, is the basis for determing the centroid in η for each tower. In addition, for the central calorimeter, the azimuthal centroid for each tower component (EM or hadronic) is determined from the relative energy measured in the phototubes which bracket the tower.
[10] J. Alitti et al., CERN Report No. CERN-PPE/90-105 (1990), submitted to Z. Phys. C.
[11] F. Abe et al., Phys. Rev. Lett. **65**, 968 (1990).
[12] The PAPAGENO event generator was used, I. Hinchliffe, private communication.
[13] R. Field and R. Feynmann, Nucl. Phys. B **136**, 1 (1978).
[14] A modified version of the ISAJET fragmentation scheme was employed, F. Paige and S. Protopopescu, Report No. BNL-38034, 1986 (unpublished); and in *Physics of the Superconducting Super Collider, Snowmass, 1986*, Proceedings of the Summer Study, Snowmass, Colorado, 1986, edited by R. Donaldson and J. Marx (Division of Particles and Fields of the APS, New York, 1987), p. 320.
[15] T. Hessing, Ph.D. thesis, Texas A&M University (1990); CDF collaboration, F. Abe et al., to be submitted to Phys. Rev. D.
[16] Z. Kunszt and E. Pietarinen, Nucl. Phys. **B164**, 45 (1980); T. Gottschalk and D. Sivers, Phys. Rev. D **21**, 102 (1980); F. Berends et al., Phys. Lett. **118B**, 124 (1981).
[17] J. Collins and D. Soper, Phys. Rev. Lett. D **16**, 2219 (1977).
[18] cf. S. Ellis, in *The Santa Fe TASI-87*, Proceedings of the 1987 Theoretical Advanced Study Institute in Elementary Particle Physics, Santa Fe, New Mexico, 1987, edited by R. Slansky and G. West (World Scientific, Singapore, 1988), p. 274.
[19] M. Mangano and S. Parke, Phys. Rep. **200**, 303 (1991).
[20] E. Eichten, I. Hinchliffe, K. Lane, and C. Quigg, Rev. Mod. Phys. **56**, 579 (1984).
[21] M. Diemoz, F. Ferroni, E. Longo, and G. Martinelli, Z. Phys. C **39** (1988), 21 (sets 1, 2, and 3).
[22] F. Abe et al., Phys. Rev. D **44**, 29 (1991).